Influence of cold rolling on *in vitro* cytotoxicity and electrochemical behaviour of an Fe-Mn-C biodegradable alloy in physiological solutions

Malcolm Caligari Conti [a], Daniel Aquilina [a], Carlo Paternoster [b], Daniel Vella [a], Emmanuel Sinagra [c], Diego Mantovani [b], Glenn Cassar [a], Pierre Schembri Wismayer [d], Joseph Buhagiar [a,*

[a] *Department of Metallurgy and Materials Engineering, University of Malta, Msida, MSD 2080, Malta*

[b] *Laboratory for Biomaterials and Bioengineering, CRC-I, Department of Mining, Metallurgical and Materials Engineering & CHU de Quebec Research Centre, Laval University, Quebec City, Canada*

[c] *Department of Chemistry, Faculty of Science, University of Malta, Msida, MSD 2080, Malta*

[d] *Department of Anatomy, Faculty of Medicine and Surgery, University of Malta, Msida, MSD 2080, Malta*

[*] Corresponding author.

E-mail address: joseph.p.buhagiar@um.edu.mt (J. Buhagiar).

Abstract

The properties of cold-worked Fe-13Mn-1.2C steel, as candidate material for scaffolding and stenting applications, have been investigated. The study of the electrochemical corrosion susceptibility of Fe-13Mn-1.2C alloy in protein bearing and non-protein bearing physiological solutions, revealed that there were no differences between the as-received, 10% and 20% cold worked Fe-13Mn-1.2C samples. Although protein addition reduces the overall corrosion rate in static immersion degradation tests for both the cold worked and non-cold worked alloys, there were no discernible differences in the corrosion rates of samples with different percentages of cold work deformations. Similarly, potentiodynamic testing showed no differences between the corrosion rates in solutions with and without protein addition. Atomic absorption spectroscopy (AAS) results—post static immersion—showed similar values of Fe and Mn concentrations in the

electrolyte for all the investigated conditions. Cold working was found to increase Grain Average Misorientation (GAM) and deformation twins within the steel, and, consequently, this led to an increase in the elastic modulus. Hence, cold-rolling may be used to achieve smaller sections (volumes) in order to support the equivalent load of the non-cold worked counterpart, giving a larger surface area to the volume ratio, thereby increasing the corrosion rate, and, in turn, rendering the degradation process shorter. When considering cytocompatibility *in vitro*, the collected supernatant particulate free Fe-13Mn-1.2C steel electrolytes were seen to be equally cytocompatible with no differences being observed between the different percentage cold work conditions. The presence of solid 80 μm size particles in the seeded elutions were seen to change the results and render the Fe-13Mn-1.2C steel non-cytocompatible.

Keywords: Materials chemistry, Electrochemistry, Analytical Chemistry, Metallurgical engineering, Mechanical engineering, Materials science

1. Introduction

In recent years, a number of studies have presented the viability of using Fe-Mn based alloys for biomedical applications [1, 2]. These alloys have shown great potential in applications for biodegradable implant material. The majority of research has been focused on the use of this alloy in the construction of biodegradable cardiovascular stents. However, in recent years a new interest has risen in the use of Fe-Mn based alloys for biodegradable orthopaedic applications as suggested by Heiden et al. [3].

Biodegradable scaffolds and stents are a paradigm shift in the prosthetics industry owing to the market requirement to find an alternative to permanent prosthetics, which often require removal and revision surgery. These procedures often have personal, social and economic implications, which compromise the patient's quality of life. Traditionally, highly corrosion resistant materials such as AISI 316L, cobalt chromium alloys, nickel titanium (Nitinol), and titanium alloys amongst others, have been used for permanent prosthetics [4, 5, 6, 7]. The first materials developed for bioresorbable prosthetics were polymers and bioresorbable ceramics. The most prominent polymeric materials studied were poly-l-lactic acid (PLLA) and poly (lactic-co-glycolic acid) (PLGA) based polymers. Polymers exhibit excellent bioresorbability through the process of hydrolysis, which causes structural and chemical decomposition. Hydroxyapatite and β-TCP are, by far, the most favoured biodegradable ceramic materials. Bioresorbable ceramics are composed of bioactive inorganic materials, which, in turn, are capable of interacting with physiological fluids and bonding to bone through the formation of bone-like hydroxyapatite layers. This leads to broad biocompatibility of the scaffold and the resultant implied

interaction of the said scaffold directly with the *in vivo* environment [8]. However, both polymers and ceramics suffer from poor mechanical properties and inadequate degradation rates [8], and for these reasons, researchers are now focusing more on biodegradable metals as solutions to biodegradable scaffolds. The most studied alloy systems include the Fe-based and the Mg-based alloys [1, 9, 10]. Magnesium corrodes too quickly to provide satisfactory performance *in vivo* [11, 12] as it degrades faster than the average bone growth [13]. It is for this reason that a switch to iron-based alloys has been considered.

Hermawan et al. [1, 9, 14, 15] were the first to investigate the effects of alloying on iron-based biodegradable stents. Numerous studies have been carried out to choose the optimum alloying element. Manganese and nickel had been identified as the two most promising alloying elements since both are austenite stabilisers in Fe-Mn-C alloys, thus enabling the development of antiferromagnetic alloys, which are compatible with magnetic resonance imaging (MRI) [16]. Manganese additions were deemed superior to nickel due to the latter being known to be carcinogenic when released into the in vivo environment as also classified by the International Agency for Research on Cancer (IARC) [15]. In contrast, manganese is an essential trace element found in the human body [17, 18]. Nevertheless, manganese additions cause a deterioration of the cytocompatibility of the alloy within an *in vitro* medium. Concentrations of Mn and Fe-Mn powder have shown to decrease metabolic activity [1], although the flux of ions released from Fe-Mn alloys in physiological solutions *in vitro* have been shown to fall below the threshold for human toxicity [14].

Fe-Mn alloys are generally known to degrade through a uniform corrosion mechanism. Corrosion is initiated at grain boundaries due to the potential difference, which exists between the grains and the grain boundaries [14]. This is opposite to what is recorded to occur in pure Fe where the resulting grain boundaries are more corrosion resistant than the grains [19, 20]. In literature, experiments have often been carried out at elevated partial CO_2 pressures in order to mimic the CO_2 concentrations *in vivo* [2]. This gives rise to the formation of $MnCO_3$ crystals, which settle on the surface of the Fe-Mn-C alloy [2]. Since $MnCO_3$ is insoluble, the formation of a manganese carbonate layer reduces the number of Mn ions present in the solution [2].

The aim of this work was to study the *in vitro* response of an Fe-13Mn-1.2C alloy with regards to corrosion and cytocompatibility, to investigate the dependence of these parameters on the microstructure and texture achieved after cold rolling to several degrees. These results were then used to assess the viability of the alloy's application as a material for biodegradable scaffolds and stents.

Literatures [9, 21, 22] show that iron-based alloys used in the orthopaedic environment suffer from a degradation rate, which is too low to meet the bone healing time of approximately 6−18 months [23]. In order for the resorbable implant to be successful *in vivo,* a reduction must be achieved in the degradation time, whilst

improving the cytocompatibility of the alloy within that environment. Cold rolling of Fe-Mn alloys has been shown to approximately double the corrosion rate [9] and to enhance the mechanical properties [24] of the alloy compared to the non-cold rolled alloy, and has been thus hypothesised to have the same effect on the Fe-13Mn-1.2C alloy used throughout this work. This increase in corrosion rate is attributed to the fact that cold rolling applied to Fe-Mn alloys generally leads to the transformation of the austenite (γ) phase to a martensite (ϵ) phase. A bi-phasic morphology then causes an increase in the corrosion rate by means of micro-galvanic corrosion acceleration [9].

The degradation time frame may also be indirectly reduced by virtue of the ameliorated mechanical properties imparted to the alloy. Yanushevich et al. [24] investigated the effect of unidirectional cold rolling on recrystallization and tensile behaviour of Fe-17Mn-1.5Al-0.3C twinning-induced plasticity (TWIP) steel. They showed that this cold deformation process caused an increase in dislocation density and led to the development of deformation twins and shear bands. The improved mechanical properties allows for lower volumes and smaller sections to be used within the *in vivo* orthopaedic and/or hematologic environment, thus increasing the surface area to volume ratio and also decreasing the mass of the material to be degraded.

The Fe-13Mn-1.2C alloy is a novel material in the field of biomedicine and, to the best of the authors' knowledge, has never been characterised before. The higher percentage of carbon allows the alloy to retain a 100% austenitic structure while having far less manganese than the commonly used Fe-30Mn and Fe-35Mn alloys [14, 25]. The reduced percentage of manganese within the alloy would lend itself well to reduced ionic percentages of manganese at the site of implantation during resorption, possibly allowing for better cytocompatibility. Thus, an increase in the corrosion rate, when compared to pure iron, should be recorded as a result of increased manganese content and the induced microstructural changes achieved by cold rolling. This is realised while also improving the cytocompatibility of the alloy by virtue of the reduced number of manganese ions eluted.

The hypothesis is that cold rolling applied to an Fe-13Mn-1.2C alloy may decrease the degradation time frame of the parent non-cold rolled alloy whilst retaining its cytocompatibility.

This work presents novel results with regards to the Electron Backscatter Diffraction (EBSD) characterisation of a unidirectional rolled Fe-13Mn-1.2C alloy. It also presents a study of the change in the mechanical properties due to the mentioned deformation. The presented microstructural changes are also related to the degradation rate of the cold rolled Fe-13Mn-1.2C alloy in protein bearing and non-protein bearing physiological media in a CO_2 rich atmosphere. Much like other works in literature, the cytocompatibility of elutions obtained from *in vitro* corrosion are studied. However, this work goes beyond simple ionic elutions to also include elutions

containing solid corrosion particles. The results can then be used to target and mini-mise the specific corrosion mechanism, which causes most harm when implanted *in vivo*.

2. Materials and methods

The Fe-13Mn-1.2C Hadfield steel used throughout this work was supplied by Polstar Metals Inc. (Ontario, Canada) in the form of 2 mm thick hot rolled plates in the annealed, quenched and austenitic state. The composition can be found in Table 1. The material was cold rolled to achieve 10% and 20% thickness reductions as described in Table 2. The thickness reduction was obtained by unidirectional rolling.

2.1. Microstructural evaluation

X-Ray diffractometry was carried out using a D8 Advance diffractometer (Bruker, USA) with a copper ($Cu_{K\alpha}$) radiation ($\lambda = 0.154$ nm) source. The disk-shaped sample analysed was cut to a diameter of 25 mm and prepared by sequential grinding and polishing steps to a finish of 0.02 μm, using OP-A suspension (Struers, Denmark). The scanning range was set to cover 2θ angles between 40° and 100° with a step size set to 0.02° and a scan speed of 0.5°/min.

As well as grain size and distribution, EBSD analyses were also carried out to characterise the microstructural texture and misorientation. These were carried out in the planes parallel (Surface 'A', Fig. 1) and normal (Surface 'B', Fig. 1) to the plane of the rolling direction of the FMC00, FMC10, and FMC20 samples. The texture study was carried out using a Field Emission Scanning Electron Microscope (FeSEM) (Merlin Gemini II, Carl Zeiss, Germany) fitted with an EBSD/EDX detector (EDAX, Ametek, Japan). The sample was tilted at 70° with respect to the EBSD detector to maximise the Kikuci lines' intensity. The working distance

Table 1. Nominal elemental composition of Fe-13Mn-1.2C in wt. %.

Element	Mn	C	Si	P	S	Fe
Composition	11−14	1−1.3	0.6	0.05	0.04	Balance

Table 2. Abbreviated sample names and their features.

Sample Name	Percentage Reduction in thickness (%)	Initial thickness (mm)	Final thickness (mm)
FMC00	0	2.0 ± 0.1	2.0 ± 0.1
FMC10	10	2.0 ± 0.1	1.8 ± 0.1
FMC20	20	2.0 ± 0.1	1.6 ± 0.1
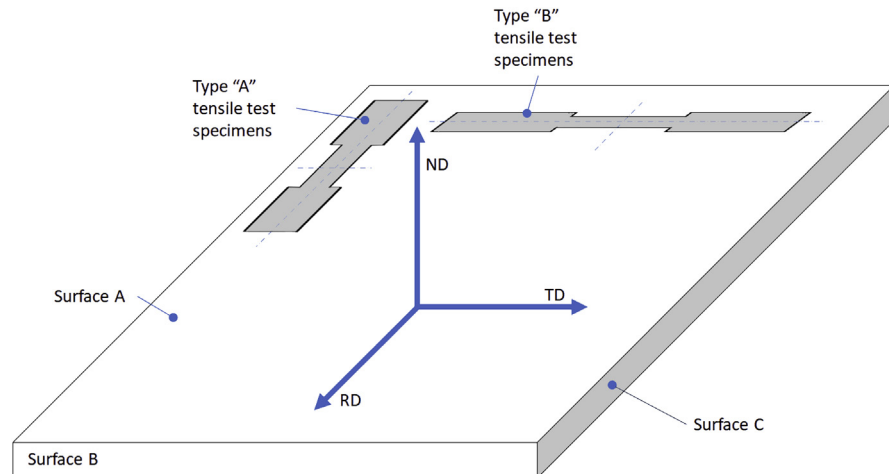
Fig. 1. Schematic of main directions. Type 'A' and type 'B' specimens have their longitudinal axes parallel to the rolling direction (RD ⊥ Surface 'B') and transverse direction (TD ⊥ Surface 'C'), respectively. Both their normal surfaces can be described by the normal direction (ND ⊥ Surface 'A').

was set to 15 mm, while the working voltage and current were set to 20 kV and 4 nA, respectively. The EBSD analyses were carried on an area of 220×220 μm with the step size set to 0.12 μm. Prior to orientation mapping, a clean-up procedure was applied using EBSD analysis software (TSL OIM, Ametek, Japan) based on grain dilation, where a minimum tolerance angle of 5° and a minimum grain size of two points were set. The minimum grain size defines the number of scan points before a group of neighbouring and similarly oriented points is identified as a grain. It was noted that after the post grain dilation procedure, the amount of data modified was less than 10%.

2.2. Mechanical testing

Tensile testing was performed using an Instron 8400 tensile tester (Instron, USA) following standard ASTM E8M-04: *Standard Test Methods for Tension Testing of Metallic Materials [Metric]*. The samples were cut using wire electrical discharge machining to specifications in ASTM E8M-04 in a direction parallel to the rolling (type 'A' tensile test specimens, Fig. 1) and perpendicular to the rolling (type 'B' tensile test specimens, Fig. 1). The cross-sectional area of the sample mid-section was then measured at five points using a micrometre screw gauge. The samples were then loaded in the tensile tester in such a way as to clamp $80 \pm 5\%$ of the end tabs taking care not to clamp the filleted section. The loading rate was then set to 1.15 MPa/s until the yield point was reached and a deformation rate of 0.05 mm/min after the yield point. The load and extension data were then recorded.

2.3. Nano-indentation testing

Nano-indentation was performed using a nano-hardness platform (Micromaterials, UK) with a Berkovich indenter using load-controlled indentation at a maximum load of 50 mN on a 25 mm disk sample finished to a 0.02 μm polish with indents being produced on Surface 'A' (Fig. 1). Ten indents were performed per sample condition and tests were carried out at 24 °C. The indenter was brought into contact with the sample at a maximum contact velocity of 0.5 μm/s. The initial contact force was 0.1 mN and this was increased at a loading rate of 0.4 mN/s to reach the required force. Upon reaching the pre-set load, it was held for five seconds − thus allowing for creep − and then the load was removed at an unloading rate of 0.5 mN/s. The nano indentation data was then used for determination of the hardness of the alloy.

2.4. Electrochemical testing

Two kinds of electrochemical tests were performed; potentiodynamic tests (PDT) and static immersion degradation tests (SIDT). The solutions used for these tests are described in Table 3, which reports the exact composition of each medium. Two media were used for the static immersion and potentiodynamic test; the first was an electrolyte, based on a modified Hank's solution (HS), and the second one was composed of the same Hank's solution but including bovine serum albumin (HS + BSA).

Potentiodynamic testing was performed on 25 mm disks finished to a 0.02 μm polish using a Gamry Ref 600 Potentiostat (Gamry, USA) setup in a three-electrode configuration. The reference electrode consisted of a standard calomel electrode (SCE) inside a luggin capillary probe, while a platinum electrode was used as a counter electrode with the test samples acting as the working electrode. Each material

Table 3. Electrolytes used for electrochemical corrosion tests.

Reference	Salts	Diluent	pH buffer Addition	pH Stabilisation Addition	Protein Addition
Potentiodynamic test and static immersion degradation test					
HS	Hank's balanced salts (Sigma Aldrich H2387)	1 L of deionised water	0.35 g/L of NaHCO₃ (Sigma Aldrich)	NaOH (Sigma Aldrich)	None
HS + BSA	Hank's balanced salts (Sigma Aldrich H2387)	1 L of deionised water	0.35 g/L of NaHCO₃ (Sigma Aldrich)	NaOH (Sigma Aldrich)	1 g/L Bovine Serum Albumin (Sigma Aldrich A2153)
Potentiostatic test					
PBS	Phosphate buffered saline (PanReac Applichem A9191)	1 L of deionised water	None	None	None

condition was tested in the two electrolyte solutions described in Table 3. These solutions were prepared as per the previous experiments in literature [2].

A working area of 1 cm^2 was exposed to 300 mL of solution and a solution temperature of 37 ± 1 °C was maintained for the duration of the potentiodynamic test. The open circuit potential (OCP) was left to stabilise for 1 hour and was followed by a potentiodynamic sweep from -100 mV versus OCP to -400 mV versus SCE reference at a scan rate of 0.167 mV/s. Testing was carried out in accordance with ASTM G59: *Standard Test Method for Conducting Potentiodynamic Polarization Resistance Measurements*. Five repeats — spread out over seven days — were performed for each sample condition in order to be able to extract statistical conclusions.

The corrosion rate was calculated according to ASTM G102-89: *Standard Practice for Calculation of Corrosion Rates and Related Information from Electrochemical Measurements* using Eq. (1).

$$CR = \left(3.27 \times 10^{-3}\right) \frac{i_{corr} EW}{\rho} \tag{1}$$

where CR is the corrosion rate (mm/year), i_{corr} is the corrosion current density (μA/cm) deduced from Tafel curves, EW is the equivalent weight (27.92 g/eq for the Fe-13Mn-1.2C alloy) and ρ is the density (7.63 g/cm^3 for Fe-13Mn-1.2C) of the alloy.

The tested coupons tested were then rinsed in ethanol in an ultrasonication bath and transferred to an electron microscope (Merlin Gemini II, Carl Zeiss, Germany) for imaging.

Static immersion degradation testing was performed in order to analyse the ion release in sterile filtered Hank's solution, as described in Table 3, over a period of 14 days. The solutions were sterilised using a 0.22 μm Sterivex filter (Merck Millipore, USA). 100 mL of each solution was then placed in a sterilised 100 mL media bottle.

Coupons were cut from non-cold worked (FMC00), 10% cold-worked (FMC10) and 20% cold-worked (FMC20) steel to a 20 mm × 10 mm rectangle. The samples were ground to a finish of P1200 using Metprep silicon carbide grinding paper and stored in a desiccated environment until the start of the test. Eighteen samples were prepared in total; three for each deformation condition tested in each medium. Just before the test, the samples were weighed using a weighing balance (404A, Precisa, Switzerland) and then tied with a piece of nylon cord. The whole assembly was dipped in ethanol (70%) for one minute and suspended in the Hank's solution filled media bottle, at the approximate centre of the liquid volume. The bottles were then capped with a modified cap assembly, which included a 0.45 μm syringe filter (Sigma Aldrich, International) in order to allow gaseous exchange within the CO_2

incubator. The 18 bottles were then stored in an incubator (Leec, UK) for 14 days, which was maintained at 6 vol.% CO_2 and 37 °C.

After the 14 day period had elapsed, each of the samples were brought out of the media and the nylon string was discarded. The samples were then dried and weighed on a weighing balance (404A, Precisa, Switzerland) and were subsequently sonicated in 70% ethanol for 15 minutes. The samples were then dried and re-weighed. The sonication and weighing procedure was repeated n times until the weight recorded at time n-1 was equal to the weight at time n.

The samples were then transferred to an electron microscope for surface imaging and electron dispersive spectroscopy (EDS) map analysis. In order to reveal the thickness of the surface degraded layer corrosion scale by cross-section analysis of the samples by SEM, the samples were mounted on an aluminium taper section angle (Struers, Denmark), and the assembly was mounted in Metprep cold mount resin and ground to P4000.

The AAS was performed to assess Fe and Mn release from the alloy, and 9 mL samples from each electrolyte were extracted from each media bottle, and were centrifuged at 3000 rpm for 10 minutes. The supernatant solution was then transferred to three separate glass vials with a volume of 3 mL per vial (giving a total of 54 vials). The vials were then placed in a crystalliser and Bain-Marie heated using paraffin wax to a temperature of 90 °C. At this point, 3 mL of HNO_3 (trace metal grade, Sigma Aldrich, International) was added to each vial and the mixtures were stirred well. The bath temperature was then raised to 115 °C and was allowed to retain that temperature, causing 3 mL of the solution to evaporate until a total of 3 mL of each solution remained in the vial. At this point, the vials were extracted from the crystalliser and allowed to cool at room temperature. Each vial was then topped up by 600 μL of deionized water and 900 μL of 30% H_2O_2 (trace metal grade, Sigma Aldrich, International). The vials were once again transferred to the crystalliser and heated to a temperature of 115 °C until the excitement phase appeared. Once again, the solution was allowed to evaporate until 3 mL of the solution was left in each vial. The solution was then aspirated to an atomic absorption spectroscope (Model 3110, Perkin Elmer, USA), in order to obtain readings of the concentration of iron and manganese in the solution.

2.5. Cytocompatibility testing by potentiostatic elution

All samples were ground and polished to a finish of 1 μm polycrystalline polishing suspension. An as-received sample was then mounted on a three-electrode setup connected to a potentiostat (Reference 1000, Gamry, USA) exposing an area of 0.51 cm^2. A 50 mL sample of Phosphate buffered saline (PBS) solution (Table 3) was then poured into the vessel, and potentiostatic testing was performed at a

potential of -500 mV and -200 mV vs. SCE for 1 hr. After the time had elapsed, the solution, including debris, was poured into a 50 mL centrifuge tube and stored for use in a cytocompatibility testing scenario. The experiment was repeated until three repeatable plots were obtained.

All the repeats of the solutions obtained from the potentiostatic elution testing were transferred to an autoclave (Boxer, Ireland) and were sterilised. A measure of 6 mL of each elution from the potentiostatic testing was then split into two 3 mL aliquots and labelled 'Complete' and 'Supernatant'. One of the aliquots was transferred to a centrifuge (Eppendorf, Germany) and spun at 3000 rpm for 20 minutes. The supernatant was then decanted into another centrifuge tube and re-labelled 'Supernatant'. A measure of 300 μL of FBS and 3 μL of Penecillin Streptomycin (Sigma Aldrich, International) was then added to each solution and to two 3 mL aliquots of sterile PBS solution.

For the cytocompatibility tests, the outer wells of 8 white 96 well plates (Thermo-Fischer Scientific, International) were pipetted with 200 μL of sterile water. The remainder of the wells were then pipetted with 100 μL of cell suspension per well at a concentration of 25,000 cells/mL. The cell line chosen was an hFOB 1.19 cell line, representative of the osteoblast cells present in the *in vivo* application scenario of the final product. Four well plates were labelled 'Complete' and with days 1−4. Another four white well plates were labelled 'Supernatant' and with days 1−4. The well plates were then transferred to an incubator (Leec, UK) operated at 37 °C and 6 vol.% CO_2 and left there for 24 hours in order for the cells to attach to the well. A 100 μL measure of each 'Complete' and 'Supernatant' solution, along with the PBS solution as a non-toxic negative control, was then added in triplicate to each well plate labelled 'Complete' and 'Supernatant', respectively. Three wells were then also plated with 100 μL of 20% di-methyl sulfoxide (DMSO) (Sigma Aldrich, International) solution as a toxic positive control. The plates were then transferred back into the incubator.

After 24, 48, 72 and 96 hours, one white 'Complete' well plate and one white 'Supernatant' well plate were removed from the incubator and allowed to cool to room temperature. A measure of 100 μL of the solution of every well was removed and replaced with an equal volume of Cell Titre Glow II (Promega, USA). The well plates were then transferred to a Thermomixer Comfort plate shaker (Eppendorf, Germany) and were shaken at 400 rpm for 3 minutes. The plates were then allowed to rest for 10 minutes in a dark container and were subsequently transferred to a Mithras LB940 (Berthold, Germany) fluorescence reader. The fluorescence was then read at 485−500 nm_{Ex}/520-530 nm_{Em} and recorded.

A calibration curve was also generated by using a similar white 96 well plate and adding 100 μL of 400,000 cells/mL, 200,000 cells/mL, 100,000 cells/mL, 50,000 cells/mL, 25,000 cells/mL and 0 cells/mL. These were plated in six wells each and allowed to adhere for 9 hours. After the 9 hours had elapsed, an equal volume

(100 μL) of Cell Titre Glow II (Promega, USA) was added to each well. The well plates were then transferred to a Themomixer Comfort plate shaker (Eppendorf, Germany) and were shaken at 400 rpm for 3 minutes. The plates were then allowed to rest for 10 minutes in a dark container and were subsequently transferred to a Mithras LB940 (Berthold, Germany) fluorescence reader. The fluorescence was then read and recorded at $485-500$ nm_{Ex}/520-530 nm_{Em}.

3. Results

3.1. Microstructural characterisation

X-ray diffraction patterns for samples cold worked to 0% (FMC00), 10% (FMC10) and 20% (FMC20) can be seen in Fig. 2 and the only phase present was austenite (FCC). The diffractograms also showed that with increasing percentage cold work, the intensity of the (111), (200), (311) and (222) peaks dropped while the (220) peak intensity increased.
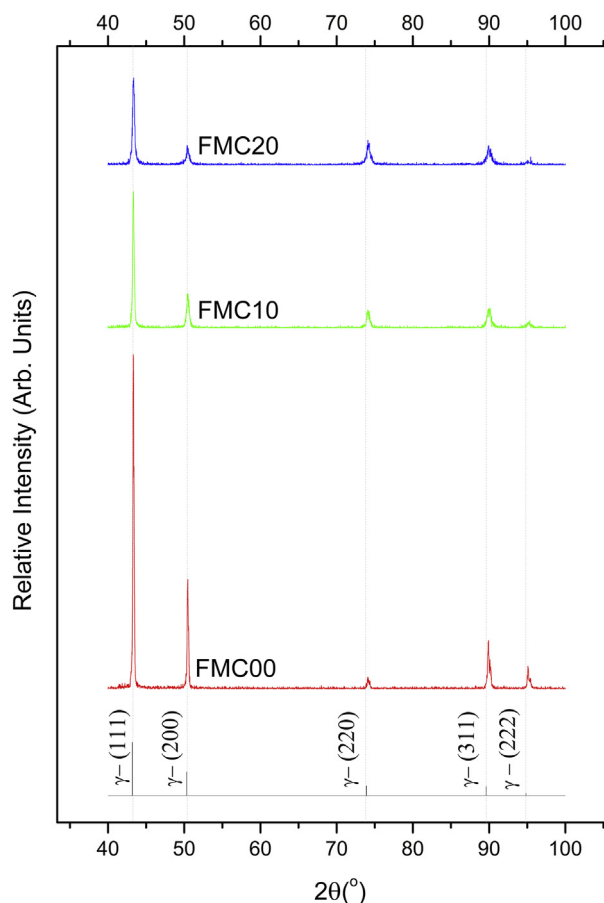
Fig. 2. Diffractogram of as-received (FMC00), 10% (FMC10) and 20% (FMC20) cold rolled Fe-13Mn-1.2C.

3.2. Mechanical properties

When considering the results in Table 4, all values of Young's modulus obtained are within error, averaging out at approximately 164 GPa. The trend for 0.2 % proof strength shows a quasi-linear increase as the amount of cold work increases, presenting significant increases in proof strength as the percentage cold work increases. Apart from the result for FMC00 the average proof strength obtained when testing type 'B' samples (Fig. 1) is always greater than the average proof strength of type 'A' samples. Both these proof strength values are, however, within error and are therefore not statistically different. The ultimate tensile strength (UTS) of the samples was seen to increase with increasing the cold work deformation percentage. No difference was observed in the ultimate tensile strength of both type 'A' and 'B' samples, as shown by the p-value results in Table 5, which are all greater than the threshold value of $p = 0.05$. The hardness of the samples increased as the percentage cold work deformation increased. The strain at break of each of the samples decreased as the percentage cold work increased from an average of approximately 60% strain for FMC00 down to an average of approximately 30% strain for FMC20, with no differences being recorded between type 'A' and type 'B' samples with the same amount of plastic deformation.

3.3. Electron backscatter diffraction

EBSD inverse pole figure (IPF) maps, presented in Fig. 3, show that as the cold work percentage increased, the amount of different textures inside a grain or crystallographic domain (micro-texture) also increased. When considering non-cold rolled samples, each grain had almost no variation in the micro-texture. On the other hand, at the higher cold work percentages, there was a clear development of a wide range of different crystallographic orientations within the same grain. Plastic

Table 4. Mechanical properties of FMC00, FMC10, and FMC20 both for type 'A' and type 'B' samples. Values are given for n = 4 samples showing the full range as error.

Sample	Young's Modulus	0.2% Proof	UTS	Hardness	Strain at Break
	(GPa)	(MPa)	(MPa)	(GPa)	%
FMC00 type 'A'	163^{+14}_{-8}	382^{+87}_{-55}	978^{+115}_{-111}	4.4 ± 0.3	58^{+9}_{-11}
FMC00 type 'B'	159^{+9}_{-9}	291^{+23}_{-23}	902^{+38}_{-38}		57^{+5}_{-5}
FMC10 type 'A'	157^{+10}_{-8}	405^{+82}_{-70}	859^{+230}_{-340}	5.7 ± 0.4	43^{+0}_{-0}
FMC10 type 'B'	167^{+19}_{-15}	462^{+49}_{-64}	1063^{+170}_{-191}		43^{+8}_{-13}
FMC20 type 'A'	178^{+24}_{-10}	464^{+134}_{-148}	1301^{+135}_{-86}	8.5 ± 0.5	27^{+6}_{-3}
FMC20 type 'B'	171^{+15}_{-26}	590^{+15}_{-22}	1232^{+41}_{-120}		31^{+3}_{-4}

Table 5. p-values from Kruskal−Wallis testing of several mechanical parameters where p-values>0.05 implies that no difference can be observed between the two datasets being compared.

	FMC00 type 'A' compared to type 'B'	FMC10 type 'A' compared to type 'B'	FMC20 type 'A' compared to type 'B'
Young's Modulus	0.564	0.297	0.917
0.2% Proof	0.083	0.180	0.117
UTS	0.248	0.297	0.917
Strain at break	1.000	0.845	0.173

deformation also led to the development of twinning defects accompanied by an increase in the grain average misorientation (Fig. 4).

From the IPF maps of the surface 'B', the grains were observed to become more elongated as the percentage cold work increased. Almost no grain elongation was observed when considering the IPF maps from surface 'A', regardless of the percentage of the cold work deformation. This is reflected in the grain size data for each of the maps in Table 6, which shows that the grain size remained constant for the maps of the grains on surface 'A', whilst the average grain size for surface 'B' decreased as the amount of plastic deformation increased.

3.4. Potentiodynamic testing

When exposed to HS and HS + BSA; FMC00, FMC10 and FMC20 exhibited an open circuit potential value of approximately -715 ± 10 mV (Fig. 5). A similar potentiodynamic trend was observed for all the studied conditions (Fig. 5) such that the current density recorded for each of the conditions was similar. A lack of difference was also observed between the corrosion rate recorded from FMC00, FMC10 and FMC20 when exposed to HS and HS + BSA (Fig. 6, Table 7). This was confirmed using Kruskal−Wallis analysis (Table 8), in which the p-values do not fall below the threshold value of 0.05.

No difference in morphology was found for FMC00, FMC10 and FMC20 after potentiodynamic corrosion testing in HS (Fig. 7). The morphology presented is representative of uniform corrosion occurring on each of the surfaces.

3.5. Static immersion degradation testing (SIDT)

Immersion testing for 14 days in HS showed that, on average, the corrosion rate for all the investigated conditions (FMC00, FMC10 and FMC20) lies at 13 µm/year (Fig. 8). The corrosion rate recorded from the same conditions in HS + BSA was observed to lie at approximately 6 µm/year (Fig. 8). When characterising the thickness of the oxide on the surface, it is clear from Fig. 9 that as the percentage cold
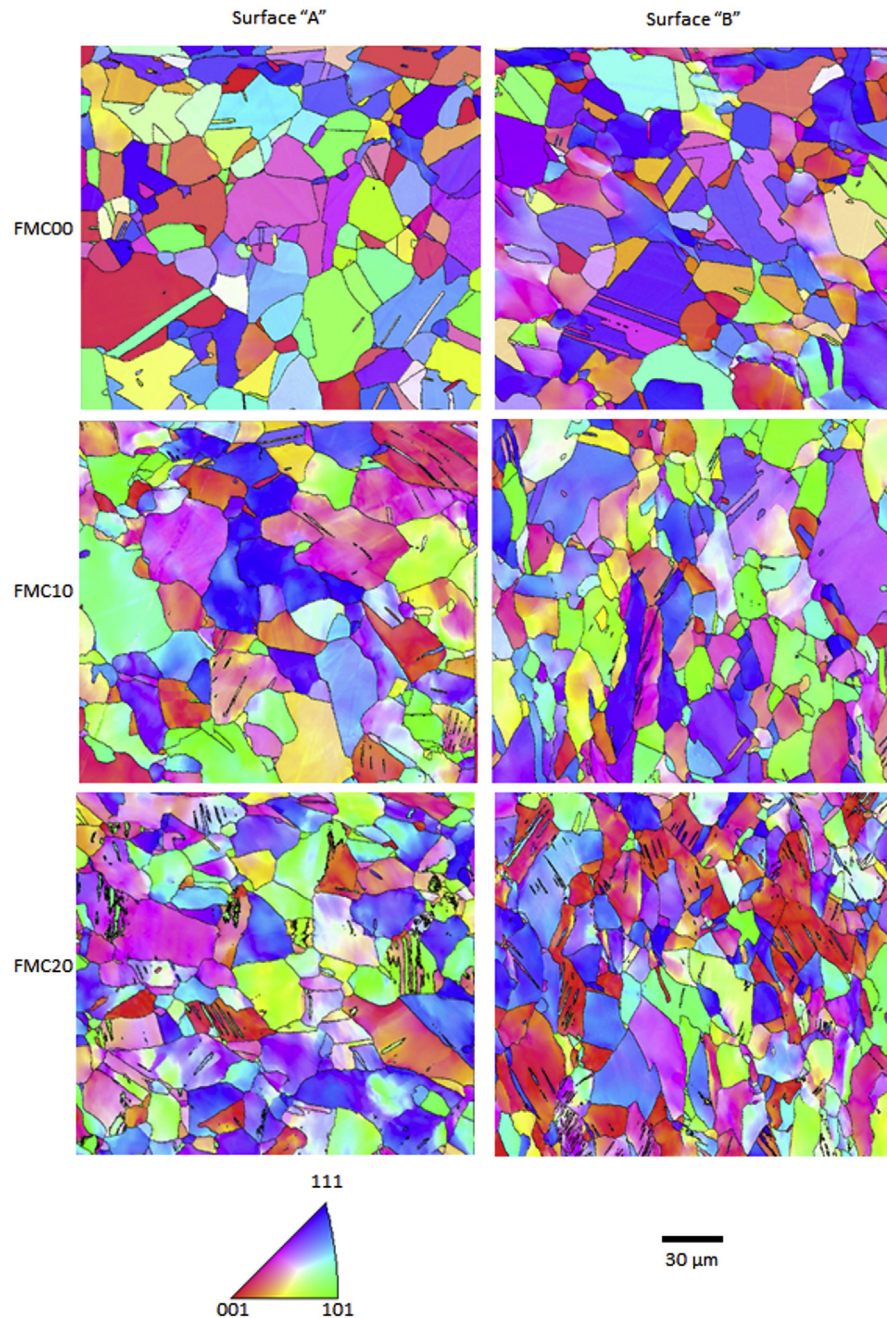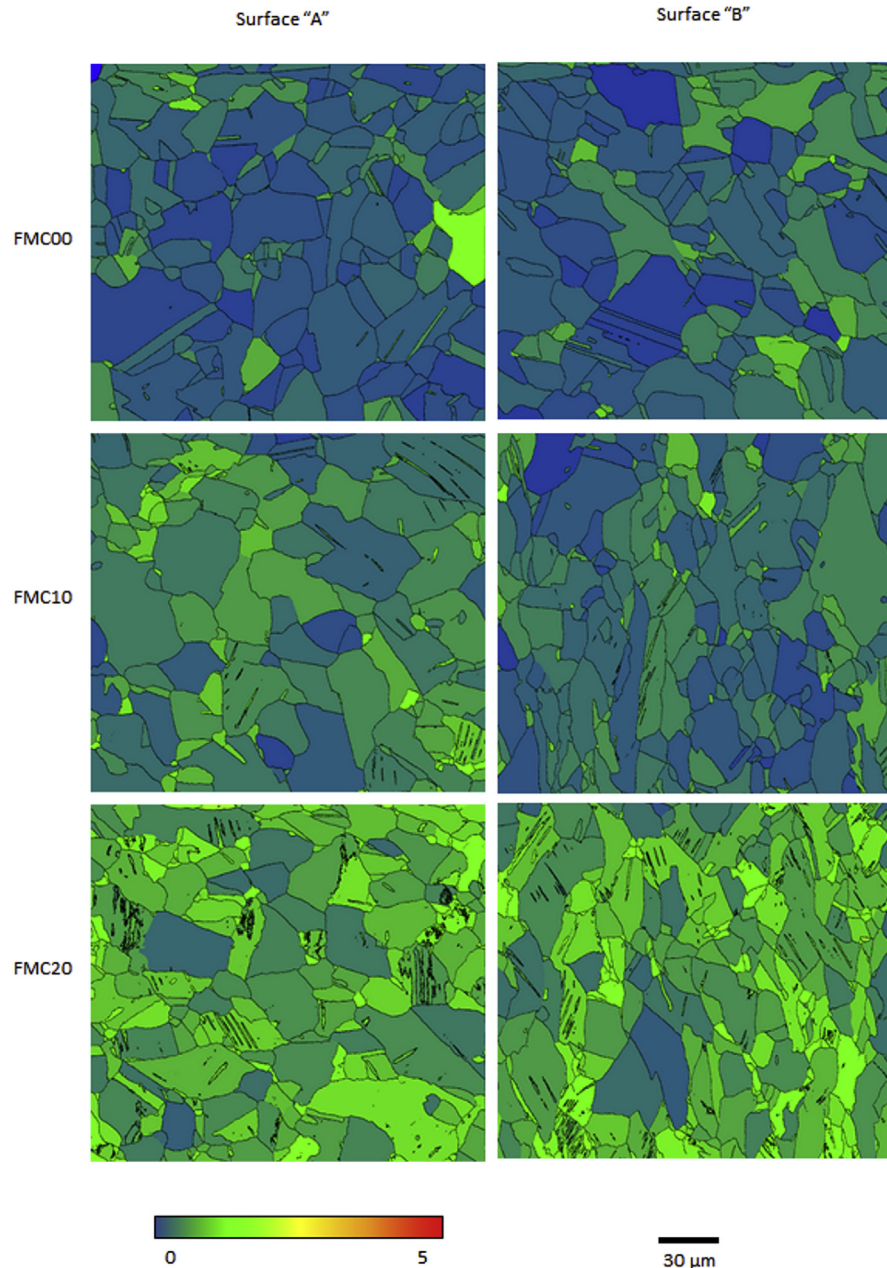
Fig. 3. Electron backscatter diffraction (EBSD) inverse pole figure (IPF) maps for FMC00, FMC10 and FMC20 scanned from surface 'A' ('parallel') and surface 'B' ('normal'). Grain boundaries highlight, solely, high angle grain boundaries with angles greater than $15°$. Each map represents an area of 220×220 μm^2.

work increases, the oxide layer retained on the surface becomes thinner in both HS and HS + BSA (Fig. 9).

Fig. 10 displays the elemental maps obtained by EDS of the surface. The maps are evidence that, when exposed to HS, the corrosion products present on the surface of

Fig. 4. Electron backscatter diffraction (EBSD) grain average misorientation (GAM) maps for FMC00, FMC10 and FMC20 scanned from surface 'A' ('parallel') and surface 'B' ('normal'). Grain boundaries highlight, solely, high angle grain boundaries with angles greater than 15°. Colour bar represents variation in colour for misorientation angles between 0° and 5°. Each map represents an area of 220 × 220 μm².

the FMC00, FMC10 and FMC20 coupons are richer in manganese, whilst those present on the surface of the FMC00, FMC10 and FMC20, exposed to HS + BSA, are rich in phosphorous as signified by the bright blue spots present on the map of the area in Fig. 10.

Table 6. Table showing grain size average in the planes parallel and normal to the plane of the rolling direction from electron backscatter diffraction scans. Errors are representative of the standard error.

|	Surface 'A' (μm)	Surface 'B' (μm)
FMC00	27.26 ± 1.30	24.60 ± 1.16
FMC10	28.40 ± 1.41	22.39 ± 1.32
FMC20	28.62 ± 1.36	19.02 ± 1.05
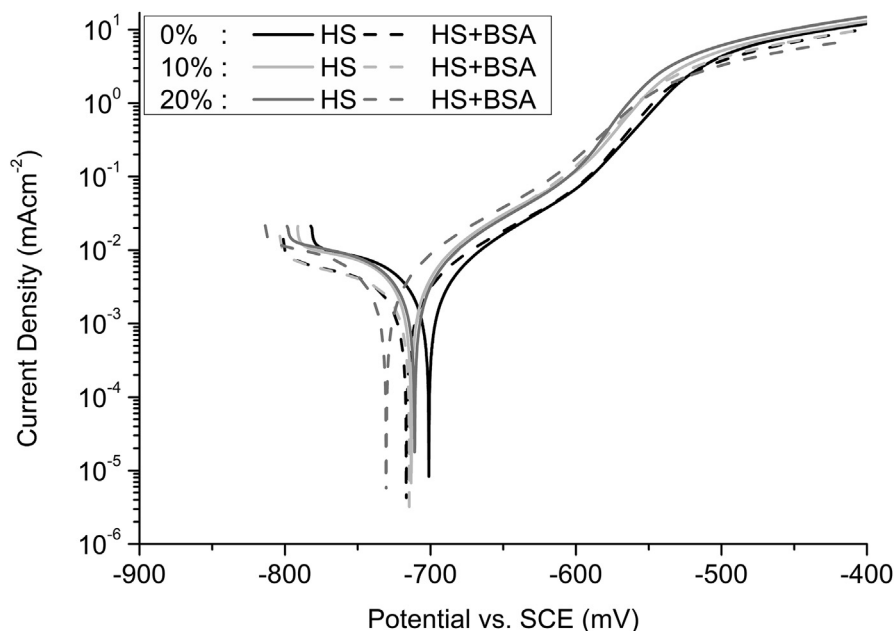
Fig. 5. Representative potentiodynamic plots of n = 5 samples for each cold work condition (0%, 10% and 20%), in different electrolytes - Hank's Solution (HS) and Hank's Solution with 0.1% bovine serum albumin (HS + BSA).

The AAS results of the supernatant solution (Fig. 11) show that the concentration of Fe in the Hank's solution obtained from FMC00 and FMC10 cold work conditions was in the region of 20 ppm−50 ppm. The corresponding Mn concentration lies in the region of 12 ppm−15 ppm. The Fe and Mn concentrations obtained from FMC20 are lower, lying at approximately 15 ppm and 11 ppm respectively. For HS + BSA the concentrations of Fe and Mn in solution for all conditions, i.e. FMC00, FMC10 and FMC20 are around 4 ppm.

3.6. Potentiostatic elution

The results from potentiostatic elution (Fig. 12) show that there is no difference in the current density recorded when FMC00, FMC10 and FMC20 were exposed to an anodic potential of -500 mV/SCE with PBS solution as an electrolyte. Analogous
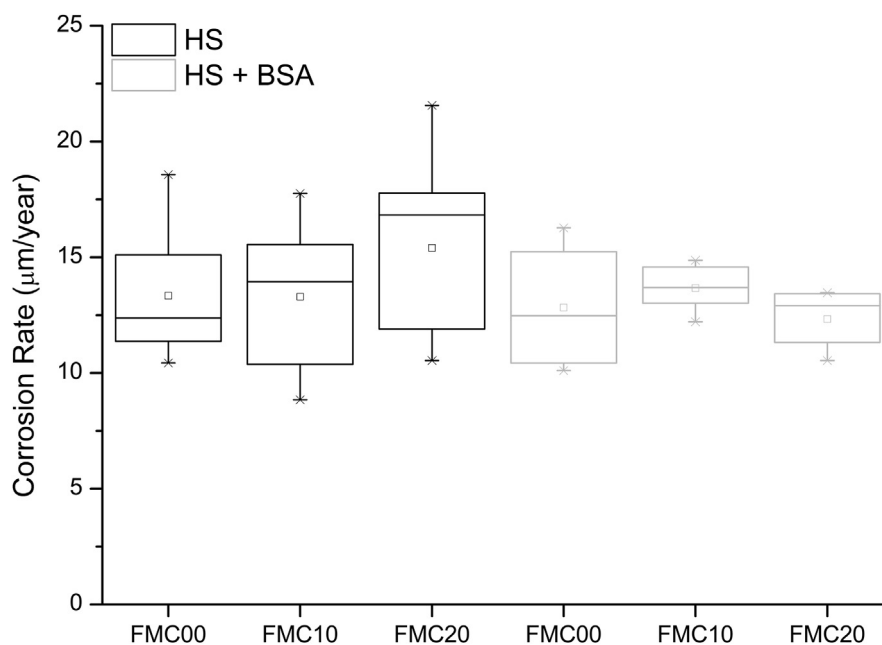
Fig. 6. Corrosion rate of n = 5 samples for each cold work condition (0%, 10% and 20%), in different electrolytes - Hank's Solution (HS) and Hank's Solution with 0.1% bovine serum albumin (HS + BSA). Box plots show first second and third quartile of the data as well as whiskers showing the total range of the data.

Table 7. Corrosion current density (i_{corr}) and open circuit potential voltage (OCP) for as received, 10% cold worked and 20% cold worked Fe-13Mn-1.2C samples in both Hank's solution (HS) and Hank's solution with 0.1% bovine serum albumin addition (HS + BSA). Errors are representative of standard error for n = 5 samples.

Cold work condition	Electrolyte solution	i_{corr} ($\times 10^{-8}$)	Calculated corrosion rate	E_{corr}
		A/cm^2	μm/year	mV/SCE
FMC00	HS	110 ± 9	13 ± 1	706 ± 44
	HS + BSA	107 ± 12	13 ± 1	720 ± 6
FMC10	HS	111 ± 9	15 ± 1	713 ± 14
	HS + BSA	114 ± 4	13 ± 1	725 ± 8
FMC20	HS	120 ± 11	14 ± 1	708 ± 37
	HS + BSA	103 ± 5	12 ± 1	715 ± 3

results were also obtained when the same material was exposed to voltages of -200 mV/SCE in the same solution.

The mass of metal lost from the coupon over 3600 s was calculated from Faraday's Law [26, 27] and plotted in Fig. 13. It was deduced that, when exposed to the same

Table 8. p-values from Kruskal−Wallis testing of corrosion rate from potentiodynamic data where p-values>0.05 implies that no difference can be observed between the two datasets being compared.

|	FMC00 HS	FMC10 HS	FMC20 HS	FMC00 HS + BSA	FMC10 HS + BSA
FMC10 HS	0.949				
FMC20 HS	0.277	0.225			
FMC00 HS + BSA	0.706	0.850	0.186		
FMC10 HS + BSA	0.291	0.806	0.685	0.624	
FMC20 HS + BSA	0.935	0.465	0.223	0.807	0.117
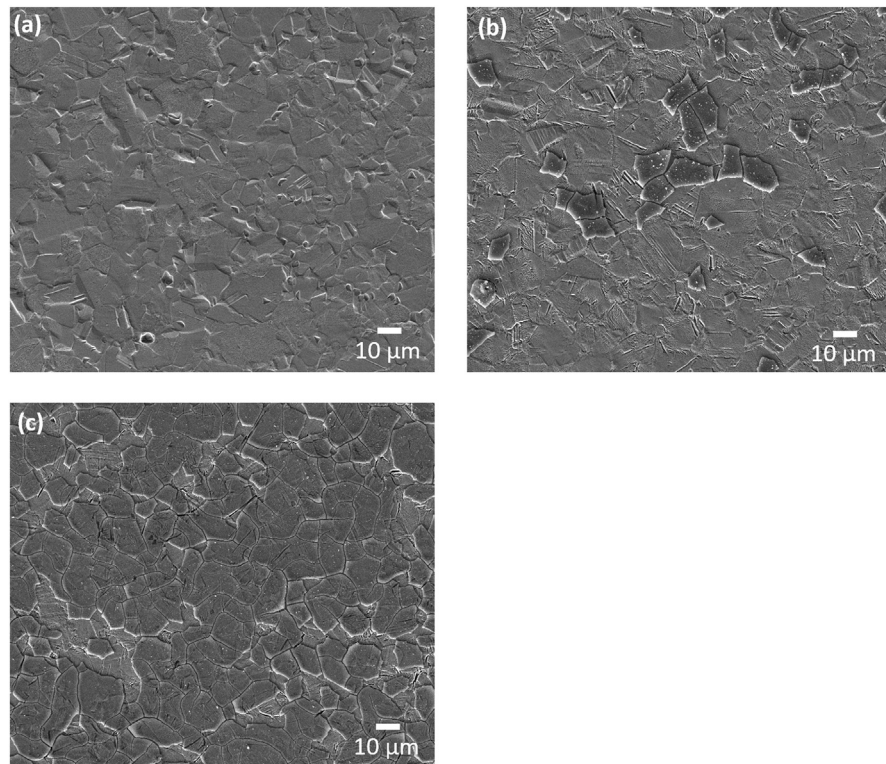
Fig. 7. SEM micrographs showing (a) FMC00, (b) FMC10 and (c) FMC20 surfaces after exposure to potentiodynamic testing in HS and subsequent rinsing and sonication in ethanol. SEM micrographs for the same samples tested in HS + BSA are not shown due to the inability to remove the BSA residue prior to imaging.

anodic potential, the values of mass lost for all percentage deformations were similar for FMC00, FMC10 and FMC20.

3.7. Cytocompatibility

The results displayed in Fig. 14(a) and (b) were obtained from similar solutions. However, whereas Fig. 14(b) represents the results of the osteoblasts exposed to
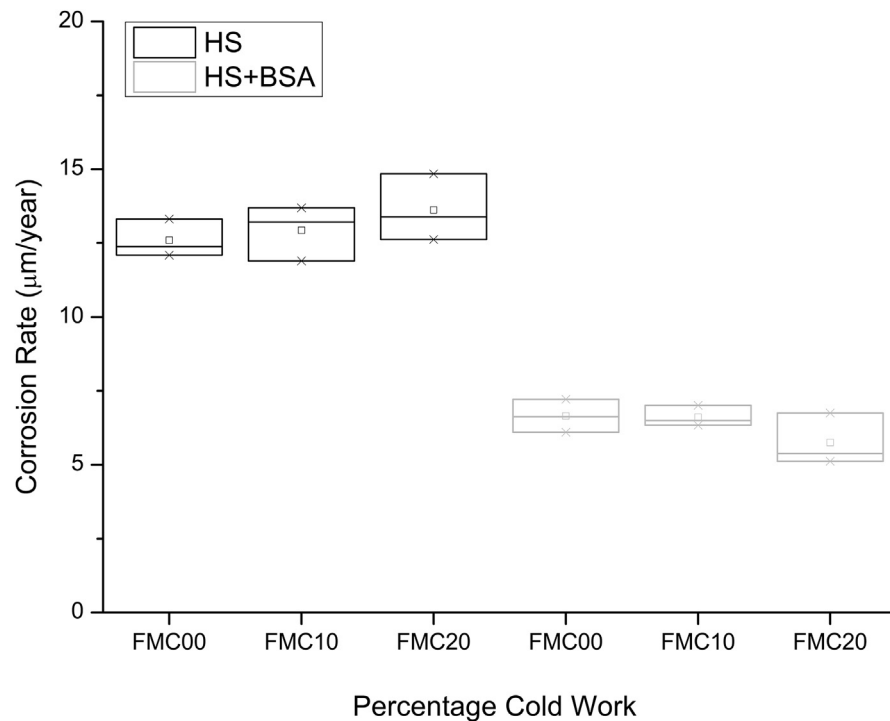
Fig. 8. Plot of corrosion rate for different percentages of cold work in HS and HS + BSA addition after a 14 day immersion experiment for n = 3 samples per condition.
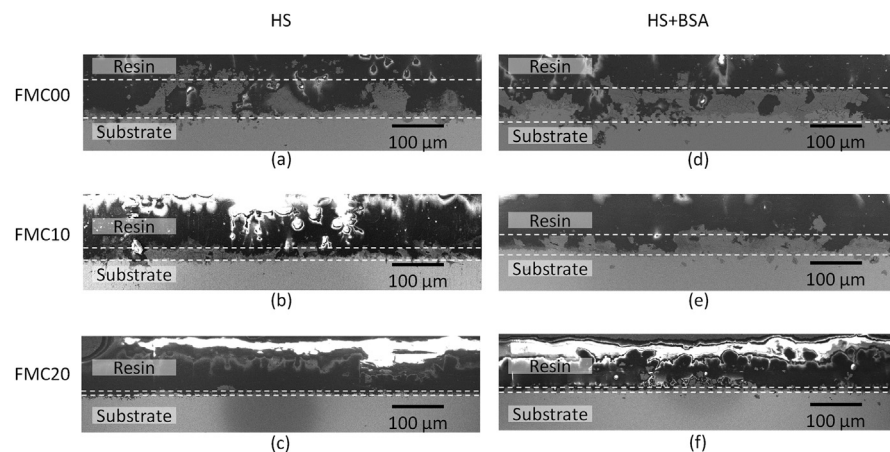

Fig. 9. Scanning electron microscopy in-lens images of oxide layer developed on the surface of (a), (d) FMC00 (b), (e) FMC10 and (c), (f) FMC20 cold worked samples after exposure to static elution in (a), (b), (c) HS and (d), (e), (f) HS + BSA. The oxide layer is marked with a dotted line and the thickness of the oxide film is magnified by 5X due to the use of a taper section angle.

the whole solution including any particulates, which may have arisen during testing, Fig. 14(a) describes the results of the osteoblasts exposed solely to the supernatant solution after centrifugation, thus being completely free of particles. The latter results are representative of osteoblast response to the Fe and Mn ionic content of the corrosion electrolyte.
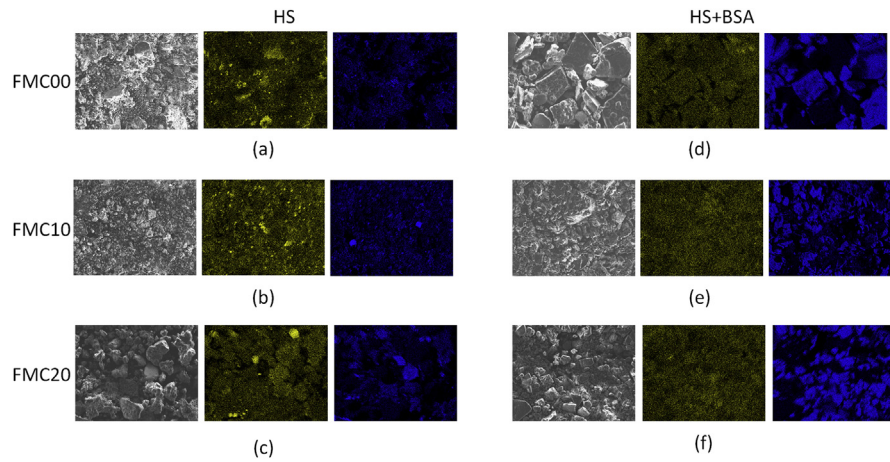
Fig. 10. EDS maps of the surface showing concentration of manganese (yellow) and phosphorous (blue) for a plastically deformed Fe-13Mn-1.2C respectively for (a), (d) FMC00, (b), (e) FMC10, (c), (f) FMC20 and exposed to (a), (b), (c) HS and (d), (e), (f) HS + BSA after immersion testing for 14 days. Each scanned area represents an area of 225 μm × 175 μm.
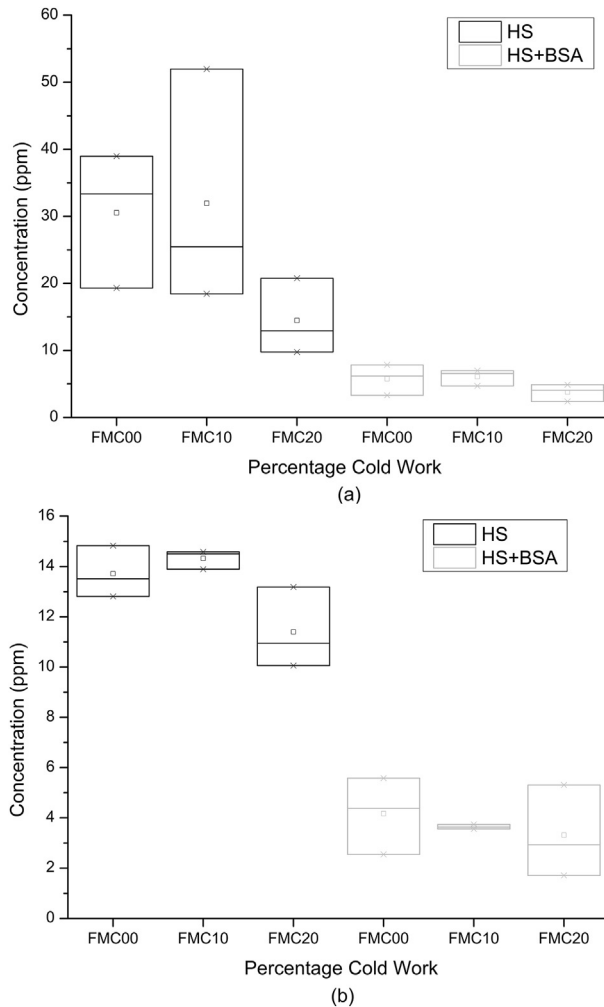
Fig. 11. Atomic absorption spectroscopy results for (a) Fe and (b) Mn from supernatant solutions of FMC00, FMC10, and FMC20 exposed to HS and HS + BSA.
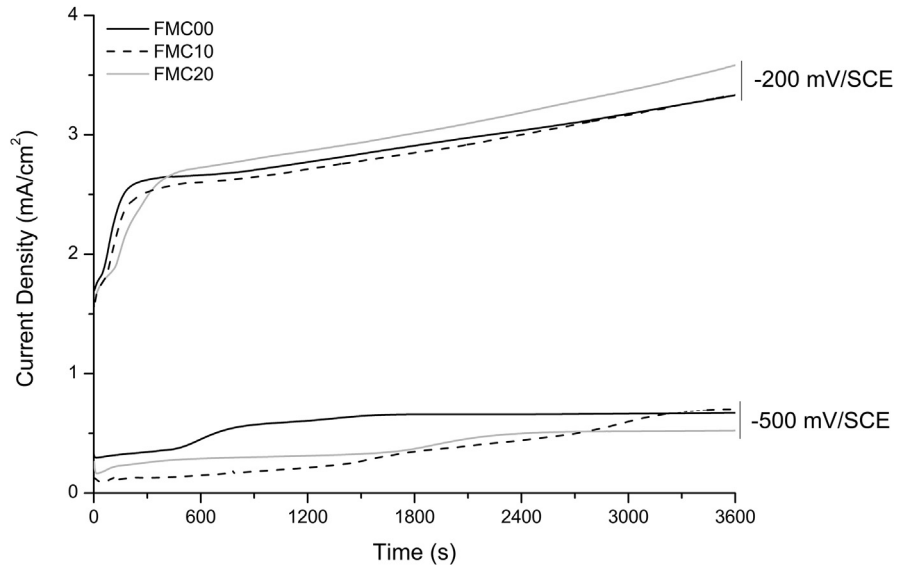
Fig. 12. Representative plots of potentiostatic elution tests on Fe-13Mn-1.2C steel at different percentages of cold work deformation at -500 mV/SCE and -200 mV/SCE for 3600 s in PBS. Each plot is representative of three similar repeats.
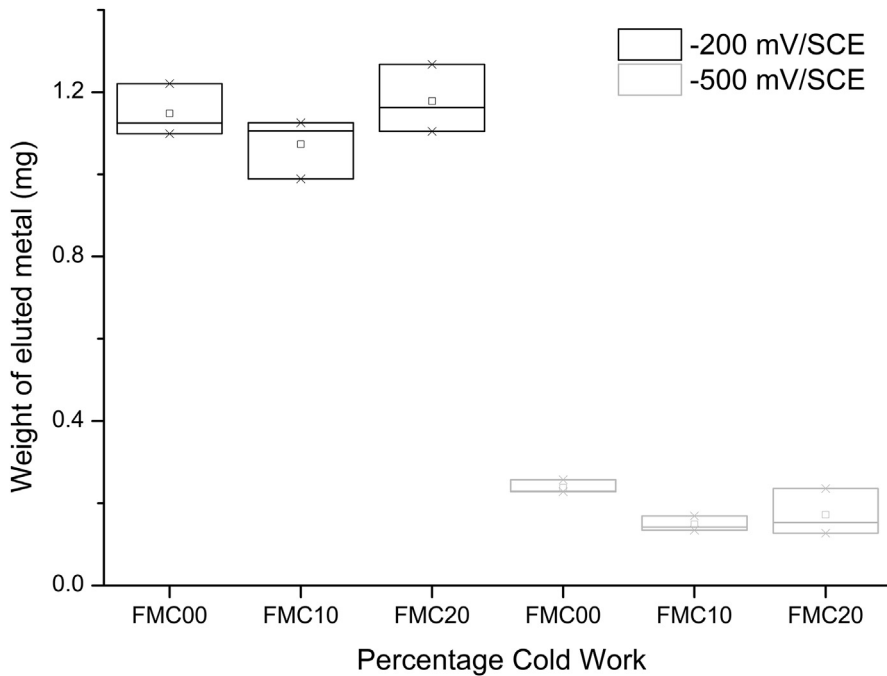

Fig. 13. Weight of eluted metal for potentiostatic elution data for different percetage of cold working deformation at -500 mV/SCE and -200 mV/SCE for 3600 s in phosphate buffered saline. Each plot is representative of n = 3 repeats.

The results of cytocompatibility testing on the supernatant solutions (Fig. 14(a)) show that the number of cells increased exponentially with time over the four days of testing in all the solutions. However, none of the solutions reached the number of cells presented by the control PBS solution. When exposed to the complete

(a)

(b)
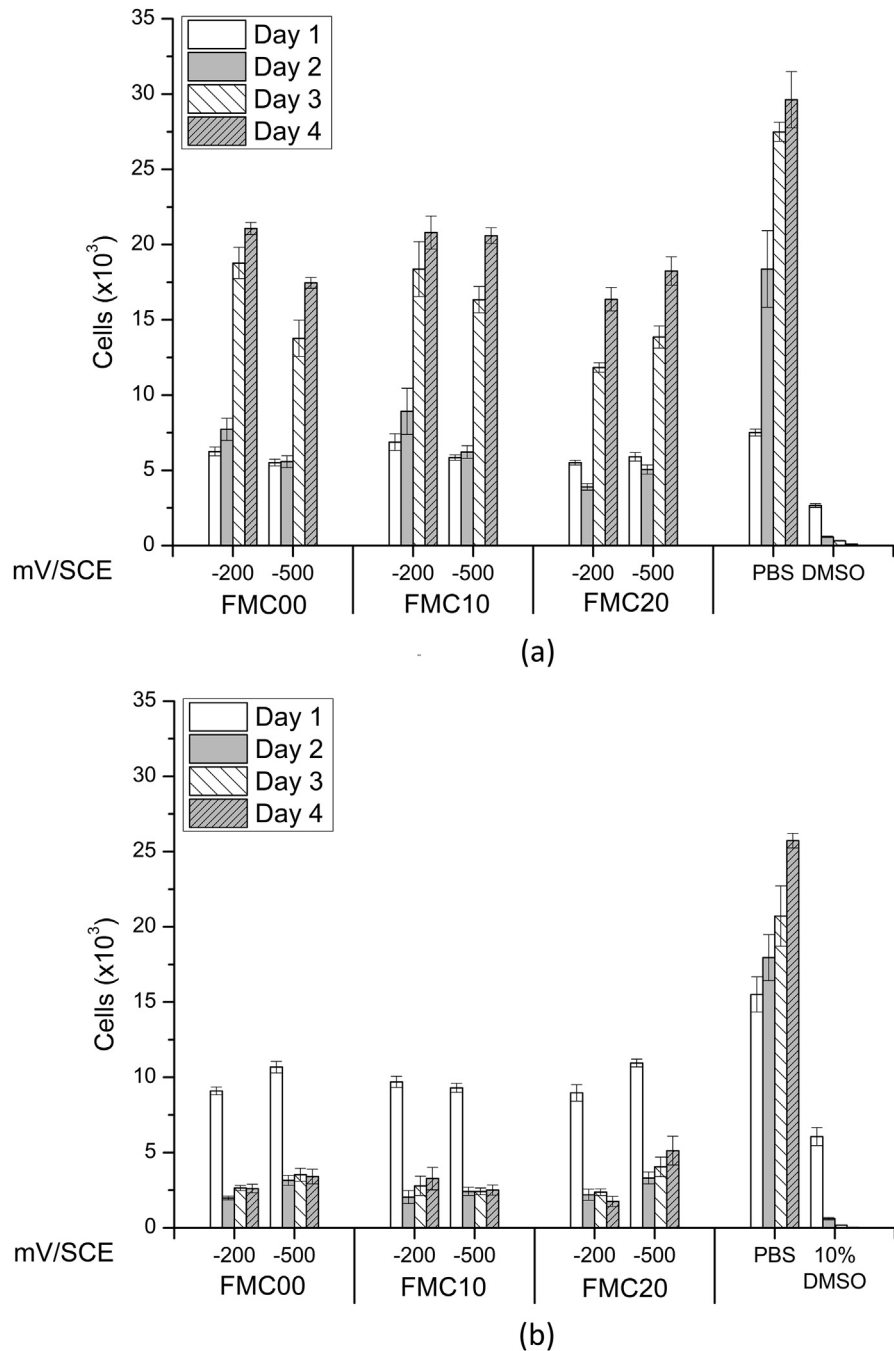
Fig. 14. Number of cells in well after exposure to (a) centrifuged supernatent elutions and (b) complete corrosion solutions from FMC00, FMC10 and FMC20 exposed to PBS at a potential of -200 mV/SCE and -500 mV/SCE. Errors are calculated as standard error for n = 9 samples.

solution, including 80 ± 9 μm particles (Fig. 14(b)), the cells were reduced in number, such that after one day, only 20% of the original number remained. This level was maintained until day 4.

4. Discussion

4.1. Effect of deformation on the mechanical properties of the Fe-13Mn-1.2C

The alloy presented in this study (Table 1) falls within the parameters set out by De Cooneman et al. [28] who state that the alloy content of twinning induced plasticity (TWIP) steels is typically 15−30% Mn, 0−1% C, 0−3 % Al, and 0−3 % Si. The same authors show that for a similar TWIP steel with a composition of Fe-18% Mn-0.6%C-1.5%Al, the Young's modulus lies at approximately 180 GPa, which is similar to the Young's modulus obtained for the Fe-13Mn-1.2C steel in this study (Table 4). Kim et al. [29] show that the same steel requires cold work of approximately 4.5%−5.5% in order to start producing twinning defects. This corresponds with the fact that in the present study, cold working to 10% plastic deformation, caused twin development in the material, which increased as the percentage deformation was increased beyond 10% (Fig. 3).

The twinning formation mechanism was accompanied by an increase in proof strength (0.2%) and the ultimate tensile strength (Table 4). This is in agreement with the work of Asgari et al. [30], who suggested that a mechanism of dislocation glide and deformation twinning caused strain hardening in TWIP steels, and thus an increase in ultimate tensile strength, since hardness has a direct relationship with tensile strength as suggested by Zhang et al. [31]. The increase in hardness and tensile strength (Table 4) coincides with an increase in grain average misorientation as the percentage deformation increases (Fig. 4) − grain average misorientation and hardness are known to be highly correlated [32].

4.2. The effect of deformation on the degradation of Fe-13Mn-1.2C steel

The potentiodynamic curves, as well as the static immersion results (Figs. 5 and 8), show that there is no difference in the degradation rate between FMC00, FMC10 and FMC20 in HS or HS + BSA. However, it must be noted that errors might have been present due to the sample exposure area used in this study, which might not have been optimal for measurements on the studied alloy. This might have caused the results to fall within the readability error when considering the setup and the equipment employed.

The absence of difference in the corrosion rate between the different conditions is reflected by the unchanged morphology of the degraded surfaces in Fig. 7. This result is due to the protection offered by the degradation product layer formed on the surface of the coupon, which might have stalled further corrosion, as also described by Feng et al. [33]. This outcome may also be related to the fact that the grain size at the surface of the material remained constant with the changing

cold work percentages. This implies that the total length of the grain boundaries (grain boundary density) at the surface did not change. Since corrosion rates are known to be affected by grain boundary length in ferrous alloys [34], an absence of change in the grain boundary length equates to a constant corrosion rate from the ferrous alloy. Yet another significant fact to be considered is that FMC00, FMC10 and FMC20 conditions were found to be fully austenitic, showing that cold working did not induce any new phases in the alloy. From literature, one of the major causes of corrosion rate increase is the presence of different phases within the same material, which causes micro galvanic corrosion, which, in turn, causes Fe-10Mn alloys to have a much higher corrosion rate compared to the other single phase alloys [9]. The fact that all alloy conditions are composed of a single homogeneous phase thus renders the alloy unsusceptible to this corrosion mechanism.

Although internal stresses are known to increase the corrosion rate of iron based alloys [34], observations made on similar single phase austenitic FeMn alloys with 20% thickness reduction showed nearly no change in the corrosion rate [9]. This agrees with the results from potentiodynamic testing, static immersion degradation test and potentiostatic test performed in this study and is attributed to the fact that twinning, in part, relieves internal stresses present when deforming the material through cold rolling [35].

When considering the thickness of the corrosion product layer left after immersion corrosion on the surface (Fig. 9), it was seen that the thickness of the corrosion product layer decreased when increasing the percentage of cold work, the corrosion product layer was determined to be composed mainly of oxides as determined by EDS. Thus, as the residual stress in the sample increased, as suggested by the hardness results (Table 4), a thinner oxide coating remained on the surface. The reason for this thinning might be related to the adhesion of the oxide onto the surface of the substrate material. The stresses in the deformed substrate exceeded the fracture surface energy of the oxide at any higher thickness and thus led the oxide to fail due to delamination and/or brittle fractures. This reduced the amount of oxide remaining on the surface, which resulted in a thinner oxide film [36, 37].

Fig. 11 demonstrates that, both in HS and in HS + BSA, the number of Mn ions measured in solution is much lower than the number of Fe ions. This is probably due to: (1) the original lower concentration of Mn in the Fe-13Mn-1.2C alloy and (2) the fact that many of the Mn ions released into the solution reacted with carbonate species to form a $MnCO_3$ layer on the surface of the alloy [2] with the enthalpy of formation of $FeCO_3$ and $MnCO_3$ being higher for $MnCO_3$, thus favouring formation of the latter species [38]. This strips the solution from free Mn ions, since $MnCO_3$ is insoluble [2] and leads to lower readings of Mn in solution because the solid particulates would have been centrifuged out of the solution being analysed.

4.3. Effect of protein addition on the corrosion rate of Fe-13Mn-1.2C

Potentiodynamic data (Figs. 5 and 6) showed no difference between the corrosion rates in Hank's solution with or without the addition of the bovine serum albumin (BSA). On the other hand, the weight loss in HS + BSA (Fig. 8) was seen to halve across all the percentage cold work deformation conditions when exposed to static immersion degradation tests. The result is also reflected in the AAS results of the supernatant solution (Fig. 11).

The decreased corrosion rate in HS + BSA, during the static immersion degradation tests was due to several factors. The presence of a biofilm developing on the surface due to protein additions [39] may have caused the elution of ions from the surface of the alloy to decrease. This may have been caused by the inability of the dissolved oxygen to reach the surface in the presence of the biofilm, thereby starving the cathodic part of the reaction [40, 41, 42, 43], which, in turn, would have led to a deceleration of the anodic reaction, leading to a reduction in metal ion dissolution. Additionally, the deposition of insoluble iron phosphate compounds on the surface of the metal (Fig. 10) may have prevented dissolution of the metallic ions into the electrolyte, acting as a barrier to further corrosion. This is in agreement with the theory presented by Lewis et al. [44] who stated that the presence of phosphate species on the surface create a barrier to charge transfer. These insoluble phosphate salts were present in reduced quantities on the surface of the metal exposed to Hank's solution without the addition of BSA, and thus the effect was less pronounced.

The absence of difference (Kruskal−Wallis, $p < 0.05$) observed between the two conditions (with and without protein) when tested in a potentiodynamic setup is likely to be a result of the anodic potential at the surface, which promotes competitive adsorption [45]. The albumin molecules binding to the ions on the surface allows them to transport the metal ions away from the solution surface interface, effectively breaking the biofilm, resulting in a higher release of ions into the electrolyte [45]. This is therefore counter to the effect that proteins have on the cathodic reaction, and may thus cause the effects to nullify each other.

4.4. Effect of cold work on the cytocompatibility of corrosion products

The *in vitro* cytocompatibility results assessing the corrosion products of Fe-13Mn-1.2C (Fig. 14 (a) and (b)) show that the responses of human foetal osteoblasts (hFOB 1.19) to elutions from metals deformed to different percentages of cold work are similar.

When exposed to the ionic content of the elution (with particles removed), the cells increased in number with time, such that by day 4, the cell number reached a value of

approximately 20,000 cells/well (Fig. 14(a)). The trend was found to be similar to that presented by the cells when exposed to the control PBS solution, even though the reading for the number of cells at day 4 for the latter solution was far higher than the reading for the number of cells for the test solutions on the same day. This implies that although the test solutions were not cytotoxic, a reduction in the cell number rate was recorded when considering all the elutions from different percentage cold work deformation samples. The effect is due to the significant amount of ions eluted into the solution giving a total ionic concentration of 22.6 mg/L. If the ratio of the mass of ions released into the solution follows the ratio of ions present in the alloy, the concentration of Fe ions in the solution would lie at 19.4 mg/L, which is just above the IC50 value of 18.4 mg/L quoted in literature for iron ions MC3T3 osteoblasts [46].

The number of live cells decreased when the human foetal osteoblasts were exposed to solutions containing the 80 ± 9 μm particles as shown in Fig. 14(b). On day 1, the fluorescence recorded from the wells exposed to the latter solutions was similar to that recorded from the wells exposed to solutions without the 80 ± 9 μm particles, thus proving that the presence of particles did not attenuate the fluorescence signal. Each solution exhibited a drop of approximately 80% of the initial cell number by day 2. This signifies that when particles are present within the plated solution, a different response is recorded by the cells, such that the solutions could be considered cytotoxic within this specific *in vitro* scenario. This result is in agreement with the results from literature, which show that as the concentration of powder of a similar iron manganese alloy in solution increases, the metabolic activity decreases, thus proving to be cytotoxic to the cells [1]. This happens regardless of the percentage deformation of the metal from which the elution was obtained.

4.5. The joint effect of corrosion response and mechanical properties on Fe-13Mn-1.2C for stenting and scaffolding applications

Two factors allow the cold worked alloy to be considered as an improvement of the currently proposed systems for stenting and scaffolding applications: (1) The improved mechanical properties of the cold-worked specimen, including hardness, proof strength and ultimate tensile strength (Table 4), mean that for the same supported load, a smaller volume of Fe-13Mn-1.2C steel needs to be used, (2) As the cold working deformation increases, no difference (Kruskal–Wallis, $p < 0.05$) is observed in the corrosion rate of the Fe-13Mn-1.2C steel as presented in Figs. 5, 6, 8 and 12. This implies that although the corrosion rate did not increase, for the same application, less material was need to be degraded *in vivo*. This is also aided by the fact that a decreased volume gives a larger surface area to the volume ratio, which aids in accelerating the overall degradation process.

Therefore, intrinsically, the amount of time it takes to completely degrade the whole scaffold/stent would be reduced since there is a lower volume of material to be degraded by the body. This is a desirable property, since the current concerns in literature are related to the long durations of scaffold and stent degradation when considering Fe-Mn-based metals [14, 47].

5. Conclusions

The hypothesis, that cold rolling applied to an Fe-13Mn-1.2C alloy may decrease the degradation time frame of the parent non-cold rolled alloy whilst retaining its cytocompatibility has been confirmed when considering the particle-free potentiostatic elutions. The corrosion rate of the parent alloy was retained whilst the mechanical properties were improved. The amelioration of the mechanical properties were found to be due to grain elongation normal to the rolling plane and the increased grain average misorientation, both parallel and normal to the rolling direction. Thus, due to the fact that reduced volumes of material can be used in order to support an equivalent load, the overall timeframe for corrosion was reduced. This is whilst the cytocompatibility of the alloys was retained, which showed cell growth throughout the *in vitro* experimental procedure. Nevertheless, when considering particulate bearing elutions, the cytocompatibility result was overturned such that the corrosion products released by the alloy is considered cytotoxic.

The BSA additions decreased the overall corrosion of the Fe-13Mn-1.2C at any cold work percentage tested when used in physiological solutions. No effect was recorded when BSA was used with the electrolyte in a potentiodynamic testing regime. This result shows that subsequent work should employ protein-bearing solutions, which, closely represent the *in vivo* scenario more accurately.

Declarations

Author contribution statement

Malcolm Caligari Conti: Performed the experiments; Analyzed and interpreted the data; Contributed reagents, materials, analysis tools or data; Wrote the paper.

Daniel Aquilina, Carlo Paternoster: Performed the experiments; Analyzed and interpreted the data.

Daniel Vella, Emmanuel Sinagra: Analyzed and interpreted the data.

Diego Mantovani, Glenn Cassar, Pierre Schembri Wismayer, Joseph Buhagiar: Conceived and designed the experiments; Analyzed and interpreted the data; Contributed reagents, materials, analysis tools or data.

Funding statement

Competing interest statement

The authors declare no conflict of interest.

Additional information

No additional information is available for this paper.

References

[1] H. Hermawan, A. Purnama, D. Dube, J. Couet, D. Mantovani, Fe−Mn alloys for metallic biodegradable stents: degradation and cell viability studies, Acta Biomater. 6 (2010) 1852−1860.

[2] E. Mouzou, C. Paternoster, R. Tolouei, A. Purnama, P. Chevallier, D. Dubé, et al., In vitro degradation behavior of Fe−20Mn−1.2 C alloy in three different pseudo-physiological solutions, Mater. Sci. Eng. C 61 (2016) 564−573.

[3] M. Heiden, E. Walker, L. Stanciu, Magnesium, iron and zinc alloys, the trifecta of bioresorbable orthopaedic and vascular implantation - a review, J. Biotechnol. Biomater. 5 (2015) 1.

[4] M.C. Conti, A. Karl, P.S. Wismayer, J. Buhagiar, Biocompatibility and characterization of a Kolsterised® medical grade cobalt-chromium-molybdenum alloy, Biomatter 4 (2014) e27713.

[5] J. Buhagiar, T. Bell, R. Sammons, H. Dong, Evaluation of the biocompatibility of S-phase layers on medical grade austenitic stainless steels, J. Mater. Sci. Mater. Med. 22 (2011) 1269−1278.

[6] R.G.T. Geesink, K.D. Groot, C.P.A.T. Klein, Chemical implant fixation using hydroxyl-apatite coatings: the development of a human total hip prosthesis for chemical fixation to bone using hydroxyl-apatite coatings on titanium substrates, Clin. Orthop. Relat. Res. 225 (1987) 147−170.

[7] G. Rooker, J. Wilkinson, Metal sensitivity in patients undergoing hip replacement. A prospective study, J. Bone Joint Surg. Br. Vol. 62-B (1980) 502−505.

[8] L.-C. Gerhardt, A.R. Boccaccini, Bioactive glass and glass-ceramic scaffolds for bone tissue engineering, Materials 3 (2010) 3867−3910.

[9] H. Hermawan, D. Dubé, D. Mantovani, Degradable metallic biomaterials: design and development of Fe−Mn alloys for stents, J. Biomed. Mater. Res. 93 (2010) 1−11.

[10] Y.F. Zheng, X.N. Gu, F. Witte, Biodegradable metals, Mater. Sci. Eng. R Rep. 77 (2014) 1−34.

[11] P.P. Mueller, S. Arnold, M. Badar, D. Bormann, F.W. Bach, A. Drynda, et al., Histological and molecular evaluation of iron as degradable medical implant material in a murine animal model, J. Biomed. Mater. Res. 100 (2012) 2881−2889.

[12] F. Witte, V. Kaese, H. Haferkamp, E. Switzer, A. Meyer-Lindenberg, C. Wirth, et al., In vivo corrosion of four magnesium alloys and the associated bone response, Biomaterials 26 (2005) 3557−3563.

[13] M. Yazdimamaghani, M. Razavi, D. Vashaee, K. Moharamzadeh, A.R. Boccaccini, L. Tayebi, Porous magnesium-based scaffolds for tissue engineering, Mater. Sci. Eng. C 71 (2017) 1253−1266.

[14] H. Hermawan, D. Dubé, D. Mantovani, Development of degradable Fe-35Mn alloy for biomedical application, Adv. Mater. Res. (2007) 107−112.

[15] H. Hermawan, H. Alamdari, D. Mantovani, D. Dube, Iron−manganese: new class of metallic degradable biomaterials prepared by powder metallurgy, Powder Metall. 51 (2008) 38−45.

[16] E. Gorkunov, S. Gladkovskii, S. Zadvorkin, S.Y. Mitropol'skaya, D. Vichuzhanin, Evolution of magnetic properties of Fe-Mn and Fe-Mn-Cr steels with different stability of austenite during plastic deformation, Phys. Met. Metallogr. 105 (2008) 343−350.

[17] K.J. Horning, S.W. Caito, K.G. Tipps, A.B. Bowman, M. Aschner, Manganese is essential for neuronal health, Annu. Rev. Nutr. 35 (2015) 71−108.

[18] E.A. Malecki, A.G. Devenyi, J.L. Beard, J.R. Connor, Existing and emerging mechanisms for transport of iron and manganese to the brain, J. Neurosci. Res. 56 (1999) 113−122.

[19] C.S. Obayi, R. Tolouei, C. Paternoster, S. Turgeon, B.A. Okorie, D.O. Obikwelu, et al., Influence of cross-rolling on the micro-texture and biodegradation of pure iron as biodegradable material for medical implants, Acta Biomater. 17 (2015) 68−77.

[20] F. Nie, Y. Zheng, S. Wei, C. Hu, G. Yang, In vitro corrosion, cytotoxicity and hemocompatibility of bulk nanocrystalline pure iron, Biomed. Mater. 5 (2010), 065015.

[21] M. Peuster, P. Wohlsein, M. Brügmann, M. Ehlerding, K. Seidler, C. Fink, et al., A novel approach to temporary stenting: degradable cardiovascular stents produced from corrodible metal—results 6−18 months after implantation into New Zealand white rabbits, Heart 86 (2001) 563−569.

[22] A.H. Yusop, H. Hermawan, Synthesis and development of polymers-infiltrated porous iron for temporary medical implants: a preliminary result, Adv. Mater. Res. (2013) 331−335.

[23] B. Wegener, B. Sievers, S. Utzschneider, P. Müller, V. Jansson, S. Rößler, et al., Microstructure, cytotoxicity and corrosion of powder-metallurgical iron alloys for biodegradable bone replacement materials, Mater. Sci. Eng., B 176 (2011) 1789−1796.

[24] Z. Yanushkevich, A. Belyakov, R. Kaibyshev, C. Haase, D. Molodov, Effect of cold rolling on recrystallization and tensile behavior of a high-Mn steel, Mater. Char. 112 (2016) 180−187.

[25] H. Hermawan, D. Mantovani, Process of prototyping coronary stents from biodegradable Fe−Mn alloys, Acta Biomater. 9 (2013) 8585−8592.

[26] S. Mischler, Triboelectrochemical techniques and interpretation methods in tribocorrosion: a comparative evaluation, Tribol. Int. 41 (2008) 573−583.

[27] D. Landolt, S. Mischler, M. Stemp, Electrochemical methods in tribocorrosion: a critical appraisal, Electrochim. Acta 46 (2001) 3913−3929.

[28] B.C. De Cooman, Y. Estrin, S.K. Kim, Twinning-induced plasticity (TWIP) steels, Acta Mater. 142 (2018) 283−362.

[29] J. Kim, Y. Estrin, B.C. De Cooman, Application of a dislocation density-based constitutive model to Al-alloyed TWIP steel, Metall. Mater. Trans. 44 (2013) 4168−4182.

[30] S. Asgari, E. El-Danaf, S.R. Kalidindi, R.D. Doherty, Strain hardening regimes and microstructural evolution during large strain compression of low stacking fault energy fcc alloys that form deformation twins, Metall. Mater. Trans. 28 (1997) 1781−1795.

[31] P. Zhang, S. Li, Z. Zhang, General relationship between strength and hardness, Mater. Sci. Eng. A 529 (2011) 62−73.

[32] S. Dziaszyk, E. Payton, F. Friedel, V. Marx, G. Eggeler, On the characterization of recrystallized fraction using electron backscatter diffraction: a direct comparison to local hardness in an IF steel using nanoindentation, Mater. Sci. Eng., A 527 (2010) 7854−7864.

[33] X. Feng, F. Zhang, Z. Yang, M. Zhang, Wear behaviour of nanocrystallised Hadfield steel, Wear 305 (2013) 299−304.

[34] K. Ralston, N. Birbilis, Effect of grain size on corrosion: a review, Corrosion 66 (2010), 075005-075005-13.

[35] M.V. Klassen-Neklyudova, Mechanical Twinning of Crystals, Springer Science & Business Media, 2012.

[36] J. Robertson, M. Manning, Limits to adherence of oxide scales, Mater. Sci. Technol. 6 (1990) 81−92.

[37] M. Schütze, M. Malessa, D. Renusch, P. Tortorelli, I.G. Wright, R. Dooley, Mechanical properties and adherence of oxide scales, Mater. Sci. Forum (2006) 393−400.

[38] J.O'M. Bockris, A.K.N. Reddy, Modern Electrochemistry, vol. 1, Kluwer Academic Publishers, New York, 1970.

[39] M. Rudee, T.M. Price, The initial stages of adsorption of plasma derived proteins on artificial surfaces in a controlled flow environment, J. Biomed. Mater. Res. 19 (1985) 57−66.

[40] J. Farack, C. Wolf-Brandstetter, S. Glorius, B. Nies, G. Standke, P. Quadbeck, et al., The effect of perfusion culture on proliferation and differentiation of human mesenchymal stem cells on biocorrodible bone replacement material, Mater. Sci. Eng. B 176 (2011) 1767−1772.

[41] T. Kraus, F. Moszner, S. Fischerauer, M. Fiedler, E. Martinelli, J. Eichler, et al., Biodegradable Fe-based alloys for use in osteosynthesis: outcome of an in vivo study after 52 weeks, Acta Biomater. 10 (2014) 3346−3353.

[42] T. Huang, J. Cheng, Y. Zheng, In vitro degradation and biocompatibility of Fe−Pd and Fe−Pt composites fabricated by spark plasma sintering, Mater. Sci. Eng. C 35 (2014) 43−53.

[43] M. Traverson, M. Heiden, L.A. Stanciu, E.A. Nauman, Y. Jones-Hall, G.J. Breur, In vivo evaluation of biodegradability and biocompatibility of Fe30Mn alloy, Vet. Comp. Orthop. Traumatol. 31 (2018) 010−016.

[44] A.C. Lewis, P. Heard, The effects of calcium phosphate deposition upon corrosion of CoCr alloys and the potential for implant failure, J. Biomed. Mater. Res. 75 (2005) 365−373.

[45] A.I. Muñoz, S. Mischler, Interactive effects of albumin and phosphate ions on the corrosion of CoCrMo implant alloy, J. Electrochem. Soc. 154 (2007) C562−C570.

[46] Y. Feng, N. Gaztelumendi, J. Fornell, H. Zhang, P. Solsona, M. Baró, et al., Mechanical properties, corrosion performance and cell viability studies on newly developed porous Fe-Mn-Si-Pd alloys, J. Alloy. Comp. 724 (2017) 1046−1056.

[47] M. Moravej, D. Mantovani, Biodegradable metals for cardiovascular stent application: interests and new opportunities, Int. J. Mol. Sci. 12 (2011) 4250−4270.